concentration of the epitaxial layer was $3 \times 10^{18}/cm^3$, which is nearly the same as that in a base region of a high-speed bipolar transistor. The carrier concentrations of the SiC was intentionally lowered to about $5 \times 10^{18}/cm^3$, so it was the same as the underlying p-type epitaxial layer. The carrier profile means that a depletion region expands into both sides of the junction. The area of the diode was 100 μm^2. Phosphorus-doped poly-Si was inserted between poly-SiC and Al electrodes to get a good ohmic contact to poly-SiC. Figure 10 shows the current-voltage characteristics at 300 K. The value of the diode ideality factor n is 1.06 down into the picoamp range. Judging from this, the current flow mechanisms of n-SiC/p-Si heterojunction fabricated is diffusion. The reverse bias leakage current was 5×10^{-10}A at 1V. The rectification ratio at 1V is around 10^6, which shows good rectifying characteristics. This low leakage and good ideality factor indicate that space-charge layer recombination currents are negligible. The above results are quite promising for HBTs.

Conclusion

We studied polycrystalline SiC grown on Si substrates from Si_2H_6 and C_2H_2 for its possible use as a wide-bandgap emitter material in Si-HBTs. Carbon concentration was around 50% regardless of Si_2H_6 and C_2H_2 gas flow ratio under a C_2H_2-rich condition. Polycrystalline SiC can be grown at substrate temperatures above 850°C. Crystalline quality depends on the film thickness. Thinner films have preferred orientations. The bandgap of the SiC is around 2 eV at 300 K, which means that inclusions of Si grains seem to be absent from the film. By phosphine doping, resistivity can be reduced to $4.3 \times 10^{-3}\ \Omega \cdot cm$, which is as low as conventional arsenic-doped poly-Si. Up to 30 min deposition of SiC at 900°C did not change the profile of the underlying boron. The value of the n-SiC/p-Si heterojunction diode ideal factor was 1.06, indicating that current flow mechanism was diffusion. Polycrystalline SiC is an excellent candidate for wide-bandgap materials used in Si-HBTs.

Acknowledgments

We thank Dr. H. Ishikawa, Dr. Y. Furumura, and Dr. T. Yamazaki for their helpful advice and encouragement.

Manuscript submitted Nov. 16, 1988; revised manuscript received Feb. 10, 1989.

Fujitsu Laboratories, Limited, assisted in meeting the publication costs of this article.

REFERENCES

1. T. Sugii, T. Yamazaki, T. Fukano, and T. Ito, "Tech. Dig. 1987 Symposium VLSI Tech.," 35 (1987).
2. M. Ugajin, S. Konaka, and Y. Amemiya, "Ext. Abs. 19th conf. SSDM," 339 (1987).
3. H. Matsunami, S. Nishino, and T. Tanaka, *IEEE Trans. Electron Devices*, **28,** 1235 (1981).
4. Y. Furumura, M. Doki, F. Mieno, T. Eshita, T. Suzuki, and M. Maeda, *This Journal*, **135,** 1255 (1988).
5. T. Sugii, T. Ito, Y. Furumura, M. Doki, F. Mieno, and M. Maeda, *ibid.*, **134,** 2545 (1987).
6. T. Sugii, T. Ito, Y. Furumura, M. Doki, F. Mieno, and M. Maeda, *IEEE Electron. Device Lett.*, **EDL-9,** 87 (1988).
7. K. Sasaki, M. M. Rahman, and S. Furukawa, *ibid.*, **6,** 311 (1985).
8. T. Yamazaki, S. Watanabe, T. Sugii, and T. Ito, *IEDM Tech. Dig.*, 586 (1987).
9. H. Matsunami, S. Nishino, and T. Konaka, *J. Cryst. Growth.*, **45,** 138 (1987).
10. Y. Furumura, M. Doki, F. Mieno, and M. Maeda, *Trans. IECEJ*, **J69-C,** 705 (1986).

Study of Electric Field Distribution in GaAs Materials and Devices Using Electro-Optic Probing Technique

Z. H. Zhu,[1] Y. H. Lo, M. C. Wu, C. L. Pan,[2] S. Y. Wang,[3] T. K. Gustafson, and S. Wang

Department of Electrical Engineering and Computer Sciences and Electronics Research Laboratory, University of California, Berkeley, California 94720

ABSTRACT

Continuous wave (CW) and pulse electro-optic probing techniques have been applied to study the electric field distribution in GaAs material and device. We have utilized the CW electro-optic probing to measure the electric field profile of a coplanar waveguide made on a GaAs semi-insulating substrate. This probing technique can be generalized to map out the three-dimensional field distribution. In addition, the inhomogeneous distribution of deep levels in a liquid encapsulated Czochralski (LEC) semi-insulating GaAs substrate is probed. The change of deep level concentration near the GaAs substrate surface after thermal annealing is in turn detected. Using the concept of harmonic mixing, we are able to employ the pulsed electro-optic probing to measure the standing wave pattern in a GaAs coplanar waveguide with various terminations. This technique is demonstrated at microwave frequencies up to 20.10 GHz. The measured effective indexes of refraction are in good agreement with those predicted by theory.

The linear electro-optic effect, or Pockels effect, has been used in many devices, such as optical modulators, switches, reflectors, and sampling gates, etc., for years to perform various functions in the transmission and processing of electrical and optical signals. Since the beginning of this decade, the rapid development of ultrafast electronic and opto-electronic devices gives impetus to the search for new measurement techniques. The application of the electro-optic effect, combined with ultrashort pulse techniques, becomes an important technique to characterize ultrafast devices and high-speed integrated circuits (1-8). Excellent reviews of this technique and its applications can be found in Ref. (8) and (9). However, most of the electro-optic measurement previously reported were done in time domain. Much broader areas of applications including electric field probing and microwave measurement in the frequency domain will be discussed in this paper.

Electric field, potential, and charge distributions in materials, devices, and integrated circuits are matters of serious concern. To the best of our knowledge, no convenient technique is available to characterize these properties in a noninvasive and *in situ* mode with high spatial resolution. However, the optical means provides an opportunity to do so. We have developed a new technique—continuous-wave (CW) and pulse electro-optic probing for studying spatial distribution of the electric field, potential, and space charge in GaAs materials and devices. The CW electro-optic probing (CWEOP) technique has been employed to study the electric field distribution in a GaAs coplanar

[1] On leave from Department of Radio and Electronic Engineering, Zhejiang University, Hangzhou, China.
[2] On leave from Institute of Electro-Optic Engineering, Chiao Tung University, Hsinchu, Taiwan, China.
[3] On leave from Hewlett-Packard Laboratories, Palo Alto, California.

waveguide (10), the change of surface electrical properties of semi-insulating GaAs after thermal annealing (11), and the inhomogeneous distribution of deep levels in a semi-insulating GaAs crystal (12). At the same time, we have successfully applied the pulsed electro-optic probing (PEOP) technique to measure the standing wave pattern in a microwave coplanar waveguide (13, 14). In this paper, we first review the basic concept of electro-optic probing and describes the experimental setup. Various experimental results are presented in turn to demonstrate the versatility of this technique. Finally, the spatial resolution and sensitivity of measurements are discussed.

Principle of Electro-optic Probing

The interaction between light and electric field provides a way to study the distribution of electric field in any electro-optic material. Briefly speaking, the electro-optic effect refers to the change of refractive index with the electric fields in an electro-optic material. An optical beam passing through the crystal experiences a phase shift between two orthogonal components. The phase shift is converted to an amplitude variation as the beam passes through a polarizer and is detected by a photodetector. Fortunately, the electronically and opto-electronically important material GaAs is a cubic crystal but does not possess an inversion center, and thus exhibits the linear electro-optic effect. Without losing generality, we describe the principle of electro-optic probing using a GaAs coplanar waveguide sample as shown in Fig. 1 as an example.

The incident light beam with x-directed polarization propagates along the (100) axis of GaAs crystal. The beam enters the crystal in the assumed y-direction on the back side and reflects from a top electrode. The electric field $E(x,y)$ in a GaAs crystal is created by applying a dc or ac voltage across the central and side electrodes. Because the y-component of the electric field is active in the electro-optic effect, we refer to this case as the "longitudinal probing mode." Thus the single-pass phase retardation between two electrically induced birefringent axes x' and z' for an arbitrary electric field. $E(x,y)$ is given by (10, 15)

$$\Delta\Gamma_{sig} = \frac{2\pi}{\lambda} n_o^3 \gamma_{41} \int_0^d E_y(x,y)dy \qquad [1]$$

Reflected from the sample, the light beam experiences a round trip phase retardation of

$$\Delta\Gamma = \frac{4\pi}{\lambda} n_o^3 \gamma_{41} \int_0^d E_y(x,y)dy = K_o V(x) \qquad [2]$$

where $\int_0^d E_y(x,y)dy$ represents the potential difference $v(x)$ between the front and back side of the sample with some x value, d is the thickness of the sample, and $K_o = (4\pi/\lambda)$ $n_o^3\gamma_{41}$ is a material constant. The transmitted light intensity with z-polarized component (after analyzer) I is given by (15)

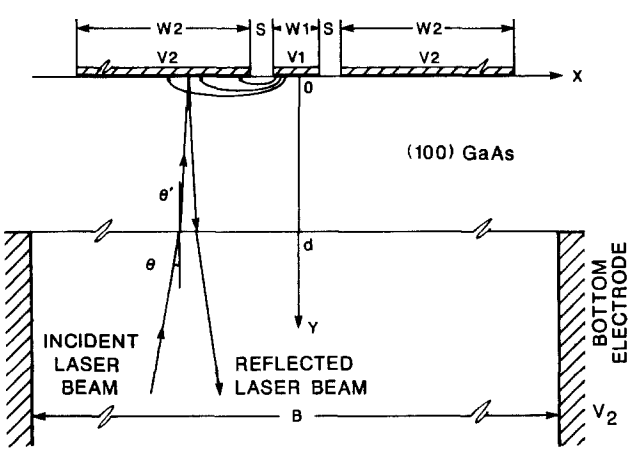

Fig. 1. Configuration of the measured coplanar waveguide sample: W_1 = 135, S = 65, W_2 = 590, d = 450, and B = 5500 μm.

$$I = I_i \sin^2\left[\frac{1}{2}(\Gamma_o + \Delta\Gamma)\right] \qquad [3]$$

where Γ_o is the static phase retardation, I_i is the incident intensity. Taking $\Gamma_o = \pi/2$, Eq. [3] becomes

$$I \approx \frac{I_i}{2}(1 + \sin\Delta\Gamma) \qquad [4]$$

Since $\Delta\Gamma$ is usually much less than one, the variation of photocurrent ΔI in a photodetector is proportional to the phase retardation $\Delta\Gamma$. The measured electro-optic signal $V_{E\text{-}O}$ is proportional to ΔI, and in turn, proportional to the phase retardation $\Delta\Gamma$. Combined with Eq. [2], the measured electro-optic signal $V_{E\text{-}O}$ can be expressed as

$$V_{E\text{-}O}(x) \propto \int_0^d E_y(x,y)dy = V(x) \qquad [5]$$

From Eq. [5] the magnitude of the measured electro-optic signal should be a function of the coordinate x. When the light beam scans along the x-direction, the profile of surface potential distribution $v(x)$ is obtained.

A more general analysis for three-dimensional internal field distribution probed by CW electro-optic probing has been presented recently (16). If certain conditions on the probing beam are satisfied, the simple linear relation between phase retardation and each field component can be established. In that coordinate system, the y-component of the polarization state $J_{\vec{yk}}$ of the probing beam is detected, and it can be approximately expressed as

$$J_{\vec{yk}} \approx \frac{K}{|\gamma|} \sum_i \left(E_{zi} - \frac{\beta}{\gamma} E_{yi}\right) \qquad [6]$$

where α, β, γ are the directional cosines of the light beam in the laboratory coordinate system. E_{yi}, E_{zi} are the y-component and z-component of electric field in ith mesh and K is a constant. To obtain Eq. [6], we must assume $\beta/\gamma \ll 1$ and $\gamma = 0$, which means that the probing beam propagates closely along the z-axis and is confined in the y-z plane. The summation in [6] is over the field components of those meshes in the optical path.

Experimental Setup

The experimental setup is shown in Fig. 2. The optical beam from an InGaAsP CW semiconductor laser (λ = 1.3 μm) mounted on an xyz stage is collimated by a microscope objective and focused on the front side of a GaAs coplanar waveguide (CPW) sample, as shown in Fig. 1. The polarization of the laser beam is aligned along one of the principal crystal axis, say the x axis. In order to operate the modulator in its linear region, a quarter-wave plate is introduced in the optical path to cause a phase shift of $\pi/2$ between two orthogonal polarization components. A low frequency driving signal (for example, 5 kHz) generates the fields in the sample. A polarizer with its polarization 90° to the incident one enables us to detect the z-polarized component from the reflected beam. The output current of

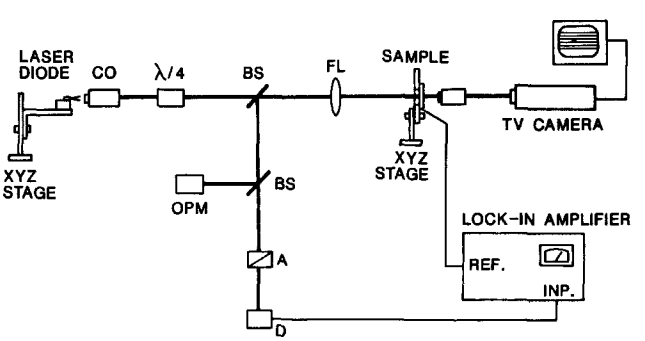

Fig. 2. Sketch of the experimental setup for CWEOP: CO, collimating objective; FL, focusing lens; A, analyzer, BS, beamsplitter; D, photodetector; OPM, optical power meter.

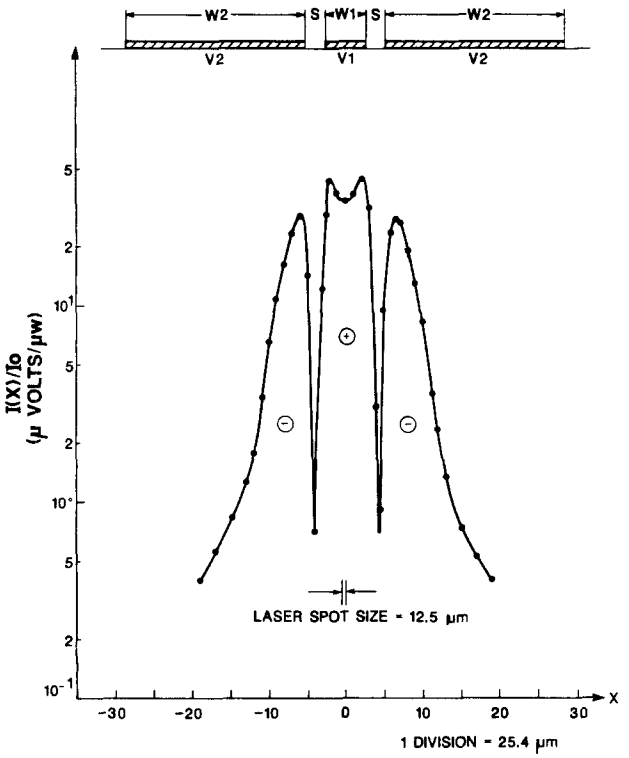

Fig. 3. Measured normalized magnitude of the electro-optic signal as a function of the beam position x.

a germanium photodetector is connected to a lock-in amplifier. The reading of the lock-in amplifier represents the magnitude of the electro-optic effect and the information of potential and field is attained from the relation in Eq. [5]. Moving the sample along the x- or z-axis, we can get the information of electric field distribution in these directions. A television camera is used to precisely monitor the position of the probing beam.

Applications of CW Electro-Optic Probing

CW electro-optic probing (CWEOP) technique is very useful in studying the electric field distribution in the following cases.

Potential distribution in GaAs CPW.—We have utilized the CW electro-optic probing technique to profile the potential distribution of a GaAs CPW sample. Scanning the laser beam along x-direction, as shown in Fig. 1, we obtain the measurement results shown in Fig. 3. The measured signal is proportional to the potential difference between the front and the back surfaces. The voltages of the ground planes and the central electrode are constant, therefore, the variation of the signal under the electrodes represents the change of potential on the back surface. In the slots between the electrodes, less reflected power is received by the photodetector due to partial transmittance of the incident optical beam. It can be corrected by normalizing the signal with the power of the reflected beam. It is noted that there is a sign change of voltages in different regions shown in Fig. 3 because the electric field lines originating on the central electrode terminate on the side electrodes.

We have carried out a theoretical analysis for a CPW using a conformal transformation (17) to find $E_y(x,y)$ in Eq. [2] and [5]. The experimental electrode configuration shown in Fig. 1 defies an analytical solution; therefore, approximations must be made. Referring to the insert of Fig. 4, we assumed the following approximate boundary conditions: $E_y = 0$ between the electrodes and $E_y = 0$ on the bottom surface $y = d$. For these conditions, the field can be found by first using the conformal transformation (10, 17)

$$T = \frac{1}{B}\,\frac{\cosh(\pi z/d) - 1 - k(A+1)}{A\cosh(\pi z/d) - A - k(A+1)} \qquad [7]$$

followed by a second transformation

$$W = \int_0^T (1-p^2)^{\frac{-1}{2}}(1-B^2p^2)^{\frac{-1}{2}}dp \qquad [8]$$

where

$$k = \frac{1}{2}[\cosh(\pi a/d) - 1] \qquad [9a]$$

$$A, B = \frac{x_1x_2 \pm 1 \pm [(x_1^2-1)(x_2^2-1)]^{1/2}}{(x_1 \pm x_2)} \qquad [9b]$$

$$x_{1,2} = -1 + [\cosh\frac{\pi}{d}(c \text{ or } b) - 1]/k \qquad [9c]$$

The field $E_y(x,y)$ thus found is used in Eq. [2] and the values of $V(x) = \int_0^d E_y dy$ are plotted in Fig. 4 as a function of x.

Comparing the calculated curve with the measured one, we find that the results are in good agreement. The change of sign of $I(x)$ in the region between electrodes is also predicted by theory as a result of the reversal in the field direction. In the outer region corresponding to the position below the two-sided electrodes, the experimental curve of $I(x)$ shows a steeper decay with distance than the calculated value of $\int_0^d E_y dy$. This minor discrepancy might be due to inaccuracy in the theoretical model in evaluating E_y in the lower half of the plane (that is, $d > y > d/2$). We thus see that this probing technique can be used a very sensitive check on the field distribution inside an electro-optic material. We also point out that the reproducibility of the measurement is excellent.

Surface properties of semi-insulating GaAs.—For GaAs integrated circuit, the quality of the semi-insulating substrate, especially the substrate surface property, is very important as it affects many aspects of device performance: threshold voltage uniformity, substrate leakage current, and the back-gating effect (18-20). Not only is the dominant deep trap EL(2) in GaAs semi-insulating substrate very nonuniformly distributed across the whole wafer, but it also tends to be depleted near the surface after thermal an-

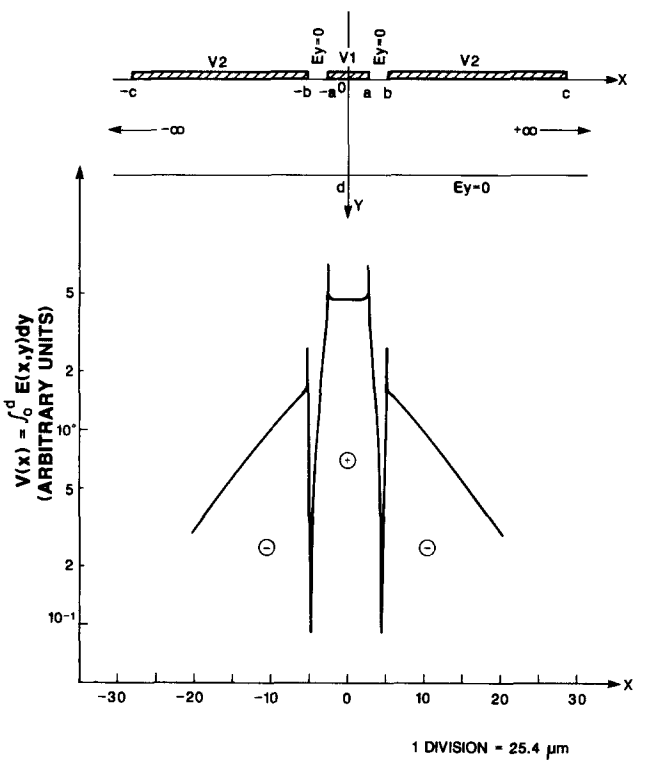

Fig. 4. Theoretical model for conformal transformation and the calculation results of the field integral V(x) for CPW: spikes at the edges of electrodes are due to the field singularity in calculation.

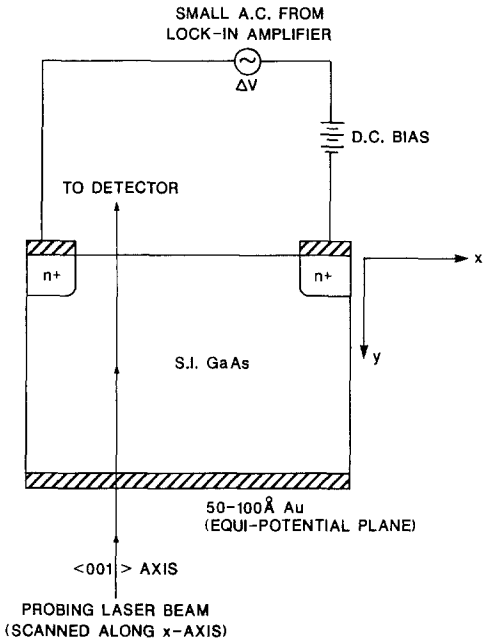

Fig. 5. Configuration of the test sample and the circuit connection in experiments of surface properties. The laser beam incident from the back side of the sample is scanned along x-axis with 0.5 μm each step. The bottom surface evaporated with gold provides the equipotential reference plane.

nealing (21, 22). The surface depletion of EL(2) traps causes a very leaky substrate surface as well as a serious backgate effect. In this section, we will discuss the use of CW electro-optic probing to detect the surface properties of a semi-insulating GaAs substrate with and without thermal annealing, and also render support for a physical model (20) describing substrate surface properties which has been speculated but up to this point not experimentally confirmed.

The experimental arrangement is similar to that shown in Fig. 2. The only difference is that we take a "transmission geometry" instead of the "reflection geometry" considered in the previous section. That implies that the transmitted beam rather than the reflected beam is detected on the front side of a sample as shown in Fig. 5. The beam spot size is focused to about 4 μm. The sample bottom is coated with a thin layer of gold (50-100Å) to maintain an equipotential plane underneath the probing area, and a small ac voltage from the lock-in amplifier reference output is connected in series with the dc bias. The detected phase retardation is proportional to the potential difference between the top surface and bottom equipotential plane, as mentioned earlier. Because the electric field right at the upper surface is principally along the x-axis, we can approximately treat the surface potential variation using a one-dimensional Poisson's equation

$$\frac{d^2V(x)}{dx^2} = \frac{-q}{\epsilon}[N_t^+(x) - N_A^- + p(x) - n(x)] \qquad [10]$$

where $V(x)$ is the surface potential with respect to the equipotential plane, $N_t^+(x)$ is the ionized EL(2) concentration, N_A^- is the background shallow acceptor concentration uniformly distributed in the substrate from carbon contamination, and n and p are the free electron and hole concentrations. Now since the lock-in amplifier can only detect the ac phase retardation generated by the electric field, N_A^-, a constant, does not contribute to the detected signal. If further, the substrate surface remains to be a highly compensated semi-insulator, the free carriers are negligible. Accordingly, a small variation of the potential from the ac signal can be represented as follows

$$\frac{d^2\Delta V(x)}{dx^2} = \frac{-q}{\epsilon}\Delta N_t^+(x) \qquad [11]$$

where the total applied small bias variation is the rms value of the ac signal. As mentioned earlier, the detected electro-optic signal $V_{E\text{-}O}$ is proportional to the applied ac voltage ΔV and as a result, the second derivative of the measured electro-optic signal is proportional to the spatial variation of the ionized trap density as described in Eq. [11]. If the space charge model is applied, the second derivative of the measured electro-optic signal, as illustrated in Fig. 6a will show a peak around the space charge boundary determined by the applied dc bias. As the dc bias increases, the peak position is expected to move toward the positive electrode, in the same way as the space charge region extends. For such a semi-insulating substrate surface, the space charge region shown in Fig. 6a is the region where all the traps are occupied or electrically neutralized, leaving only the negatively ionized shallow acceptor there (18). However, according to other experiments (22), the EL(2) level can be depleted by high temperature annealing so that its concentration could be too low to compensate the background acceptor. Based on this assumption, the sample surface will evolve as an n^+-p^--n^+ structure after annealing, and the variation of potential from the small ac signal is described as follows

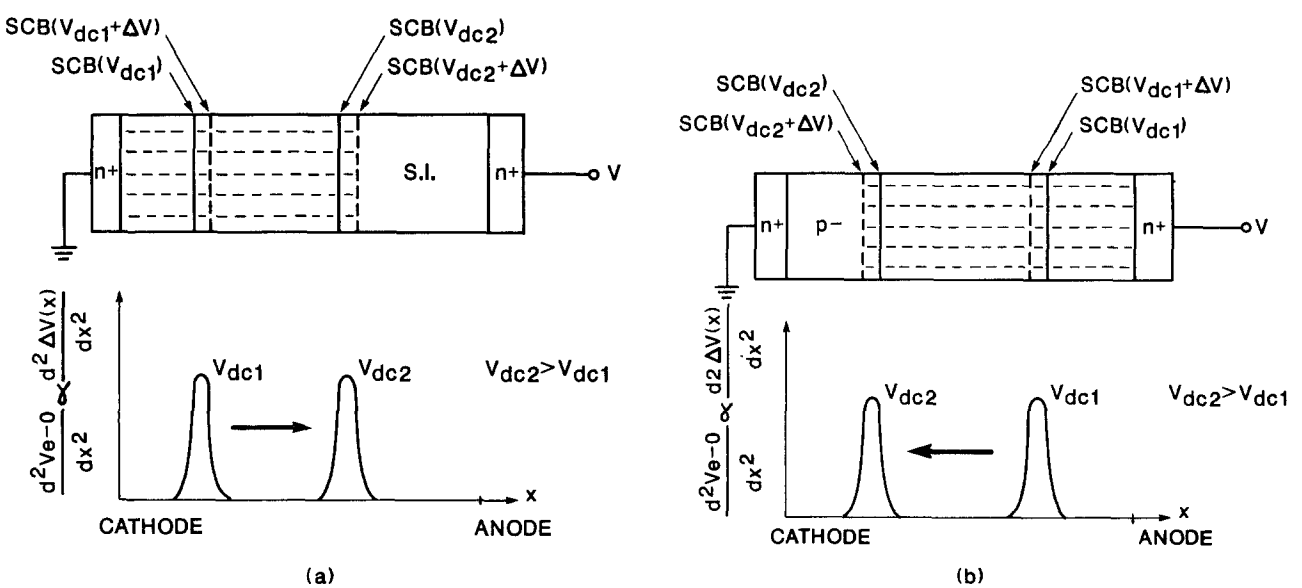

Fig. 6. The space charge distribution and the peak at the space charge boundary (SCB) appearing in the second derivative profile. Note that, with increasing bias, the peak in an n^+-i-n^+ structure (a) moves in an opposite direction to that in an n^+-p^--n^+ structure (b).

$$\frac{d^2\Delta V(x)}{dx^2} = \frac{-q}{\epsilon}\Delta p(x) \qquad [12]$$

The second derivative peak based on the space charge approximation is shown in Fig. 6b. The most prominent difference with respect to the case of a semi-insulating layer is the opposite direction of the peak movement with the dc bias. For an n^+-p^--n^+ surface structure, the peak in Fig. 6b moves toward the negative electrode with increasing dc bias because the voltage drops mainly in the reverse biased p-n junction depletion region. In contrast, the peak in n^+-i-n^+ structure moves toward the positive electrode with increasing dc bias since the voltage mainly drops in the unscreened insulating region rather than in the space-charge region. Since such a drastic difference exists between substrates with different surface properties, electro-optic signals measured at different dc bias can clearly detect very subtle changes near the surface even with a background impurity level as low as 10^{14} cm^{-3}.

In our experiment, two samples from the same GaAs liquid encapsulated Czochralski (LEC) semi-insulating substrate are prepared. One sample was annealed at 700°C for 30 min with a plasma-enhanced chemical vapor deposition silicon dioxide encapsulant; however, the other sample does not undergo any thermal annealing except for a 450°C, 1 min ohmic contact sintering. The current-voltage characteristics as shown in Fig. 7 show more than two orders higher leakage current in the annealed sample than in the unannealed one, implying the deep level surface depletion. The second derivative of the electro-optic signal with different bias voltage is illustrated in Fig. 8. Very clearly seen in Fig. 8 is that the peak under different bias moves toward the opposite directions for these two samples. Comparing the experimental results with the theoretical predictions in Fig. 6a and b, we can conclude that the unannealed substrate remains semi-insulating while the thermal annealed one evolves to have a p^- surface. Furthermore, we conclude, from this CWEOP experiment that no other electron trap on the surface possesses enough concentration to compensate the background acceptor even though many different levels have been identified from different measurements (22). If some other important trap level exists, we must generalize Eq. [10] as a multitrap Poisson's equation so that each trap should display its own peak at its own ionized boundary in the second derivative profile. The inference reveals that the CWEOP also has the potential to detect different trap levels because the second derivative profile maps each trap from its energy level into a peak in real space. The absence of other peaks in the experimental results infers that there is no other dominant trap on the substrate surface except the well-known EL(2) level.

Inhomogeneous potential distribution due to deep levels in semi-insulating GaAs substrates.—The third situation

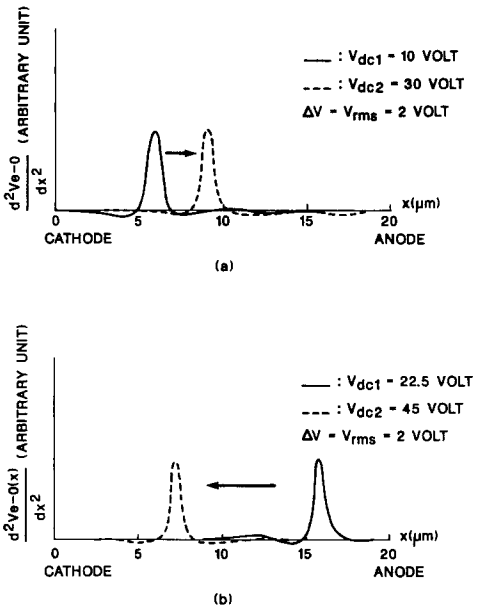

Fig. 8. The second derivative of the measured electro-optic signal for an unannealed (a) and annealed sample (b) with different bias. ΔV is supplied by the ac signal from a lock-in amplifier.

we would like to examine by this technique is the inhomogeneous potential distribution due to deep levels in semi-insulating GaAs substrates. The configuration of the sample and its circuit connection in this experiment is shown in Fig. 9. The probing laser beam scans along the longitudinal z-direction, <110> axis of the crystal. In this case, Eq. [5] should be rewritten as follows

$$V_{E\text{-}O} \propto \int_0^d E_y(y,z)dy = V(z) \qquad [13]$$

A reverse bias dc voltage source (10V) and a nanoampere meter are connected in series with the sample to measure the photocurrent.

The experimental results are shown in Fig. 10. A very interesting feature is that the longitudinal distribution of the electro-optic signal is wavy. The distance between the peaks is about 275 μm but this varies from about 200 to 500 μm depending on position. The signal variation in amplitude is about 10-15%. This spatial variation indicates that the potential distribution becomes nonuniform along the electrodes under illumination. The corresponding photocurrent I_p, which is shown in Fig. 10, is also wavy and can be correlated with the electro-optic signal. Similar experiments have been done under different frequencies (200 Hz, 5 kHz, and 50 kHz) and different bias conditions

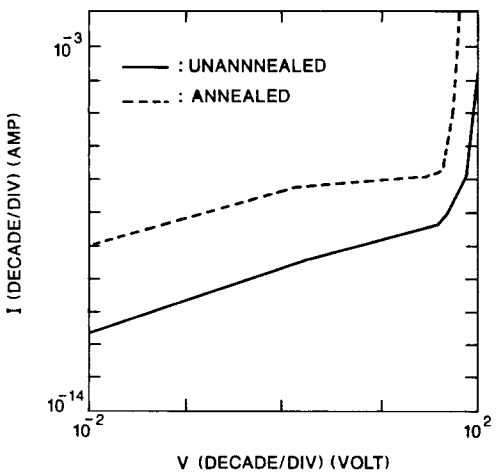

Fig. 7. Current-voltage characteristics of a sample before and after thermal annealing.

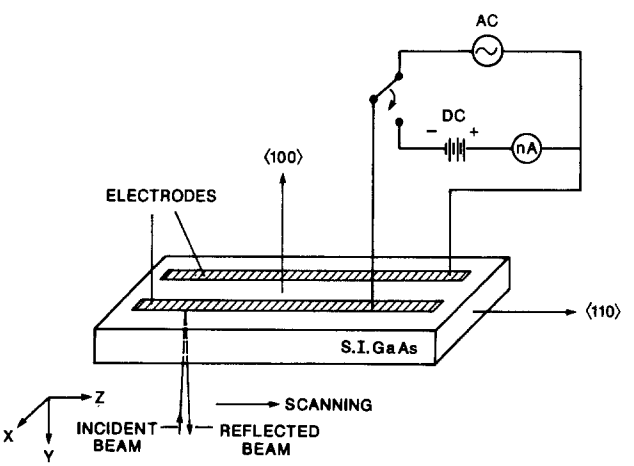

Fig. 9. Schematic diagram of the sample and circuit connection for the experiment detecting the inhomogeneous deep level distribution.

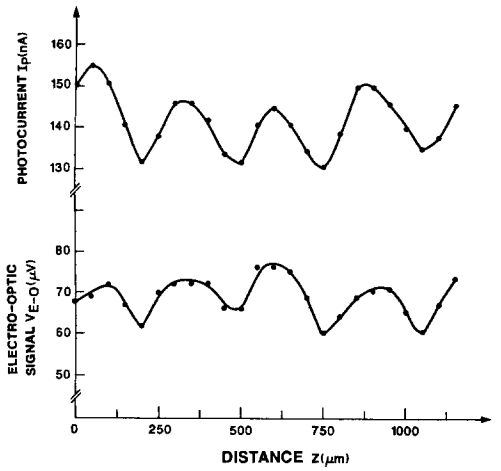

Fig. 10. Longitudinal distribution of electro-optic signal $V_{E\text{-}O}$ and photocurrent I_p.

(reverse dc bias, forward dc bias, and zero dc bias). All of the experiments show similar characteristics. The correlation between the electro-optic signal and the photocurrent suggests that the spatial variation of the measured potential is due to the excitation of deep-level traps. The electrons excited by the laser beam (photon energy = 0.95 eV) from deep levels to conduction band contribute to the photocurrent. The ionized deep levels left with positive charges change the potential on the back surface and, therefore, the electro-optic signal. Therefore, when the sample is under illumination the higher the density of the deep-level traps, the stronger the modulation of the potential and the photocurrent. The explanation is confirmed by the reported distribution of deep levels in Ref. (23). In their work, short range fluctuations on the order of a few hundred microns of infrared absorption were attributed to the nonuniform distribution of deep levels. Therefore, we believe that CWEOP technique provides a high resolution tool to probe the distribution of deep levels in semi-insulating GaAs crystals.

Pulsed Electro-Optic Probing Technique

In GaAs microwave integrated circuits, standing waves will be established if load impedance is not matched to the characteristic impedance of the waveguide. Standing wave ratio ρ is an important parameter to characterize microwave circuits. Conventional methods of measuring ρ using slotted line becomes impractical for monolithic microwave integrated circuits and, therefore, a new probing technique is needed.

Measurement of standing waves using CW electro-optic probing technique is limited by the bandwidth of photodetector. The bandwidth requirement of photodetectors can be relaxed by using harmonic mixing electro-optic probing, in which a series of short laser pulses is used as probing beam and an intermediate frequency signal is detected. This technique has the potential of measuring standing wave patterns of high RF in GaAs waveguides. Zhu *et al.* have reported the standing wave measurement in GaAs CPW at frequencies up to 20 GHz (13, 14). Standing waves in microstrip lines have also been reported (24). It should be mentioned that similar technique has also been used to study traveling wave amplifiers (25).

Principle of harmonic mixing electro-optic probing.—When a laser pulse train from a mode-locked YAG laser, modulated by an electric field, illuminates a photodetector, the photocurrent of the photodetector is proportional to the product of the light intensity and the modulating voltage. The combination of photodetector and modulator (GaAs coplanar waveguide sample in our case) can be viewed as a mixer. In frequency domain, any signal at frequency f_m propagating in the waveguide will mix with all harmonics of the fundamental repetition frequency f_o of the mode-locked YAG laser. Side bands will appear at frequency $nf_o \pm f_m$. The mixing current is given by (26)

$$i_{max} = i_{avg}\pi \frac{V_m}{V_\pi} \sum_{n=1}^{\infty} \left[\frac{\sin(\pi n f_o \tau)}{\pi n f_o \tau}\right] [\sin 2\pi(nf_o + f_m)t - \sin 2\pi(nf_o - f_m)t] \quad [14]$$

where i_{avg} is the average photocurrent, V_m is the amplitude of the modulating voltage, V_π is the half-wave voltage of the GaAs modulator, n is the order of harmonic component, and τ is the pulse width of the mode-locked laser. Insofar as the mode-locked laser as a local oscillator is concerned, the only requirement is to select a proper frequency f_m of RF signal, then we can easily measure the mixing electro-optic signal at an intermediate frequency f_i. This is given by

$$V_o \propto i_{avg}\pi \frac{V_m}{V_\pi} R_L \quad [15]$$

where V_o is the electro-optic peak developed across a load resistor R_L, and is proportional to the modulating voltage V_m.

Experimental setup.—The experimental setup is shown in Fig. 11. The pulse width of a laser pulse train with a repetition rate of f_o = 82 MHz from a CW mode-locked Nd:YAG laser (λ = 1.06 μm) is compressed to less than 3 ps to produce stronger harmonics at higher frequencies. The quarter-wave plate introduces a phase shift of π/2 between the "fast" and "slow" components of light, so that the electro-optic modulator (*i.e.*, the GaAs waveguide sample) operates in the linear region. The laser beam passing through the GaAs sample is focused to a diameter of about 8 μm on the central electrode of the coplanar waveguide. The widths of the central electrode, side electrodes, and the spacing between them are 130, 590, and 65 μm, respectively. The thickness of the substrate is 500 μm. The RF output with frequency f_m of an oscillator is fed to the GaAs coplanar waveguide (CPW) via a connector (type SMA), and the other terminal of the waveguide can be open, short, or 50Ω, so a standing wave field is established along the waveguide as the impedances are not matched. The laser beam modulated by the standing wave field is reflected from the electrode, then passes through an analyzer to convert the phase change into amplitude change. A low speed germanium photodetector is used to detect the mixing signal at the intermediate frequency f_i. A preamplifier is inserted between the photodetector and a spectrum analyzer to optimize the signal to noise ratio. A television camera is used to monitor the measuring position exactly. By scanning the laser beam from one terminal to the other terminal along the longitudinal <011> direction (*z*-axis in Fig. 11) of the CPW electrode, we can profile the standing wave pattern.

Experimental results.—Figure 12 shows the harmonic mixing electro-optic signal displayed on the spectrum analyzer by mixing the RF signal (f_m = 8.210 GHz) with the 100th harmonic component (n = 100) of the fundamental

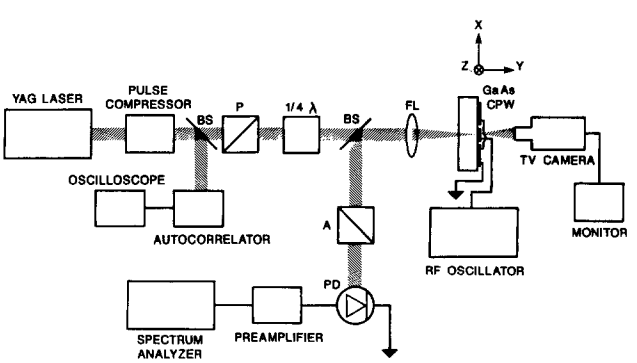

Fig. 11. Schematic diagram of the experimental setup for PEOP: P, polarizer; A, analyzer; BS, beamsplitter; FL, focusing lens; PD, photodetector.

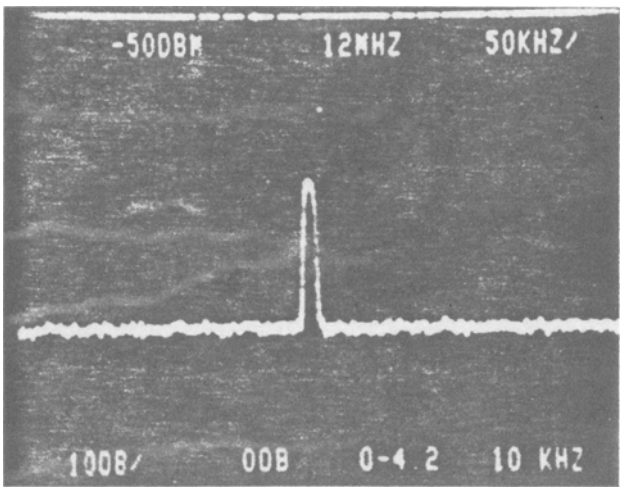

Fig. 12. Harmonic-mixing electro-optic signal (f_m = 8.21 GHz, f_o = 82 MHz, n = 100, and f_i = 10.7 MHz).

repetition rate (f_o = 82 MHz) of the mode-locked pulse. The intermediate frequency f_i of the mixer signal is equal to 10 MHz. The corresponding standing wave pattern measured is given in Fig. 13. The zero of the abscissa corresponds to the point where the measurement began, but it should be pointed out that the real zero point corresponding to the edge of the open terminal of CPW is located to the left of the zero of the abscissa. From the pattern we can see that the distance λ_{sw} between valleys is about 270 mil (≈6.9 mm) which is equal to the half wavelength of the RF signal. Substituting these data into the following formula for evaluating the effective index n_e of GaAs CPW, we have

$$n_e = \frac{c}{2\lambda_{sw} f_m} \qquad [16]$$

where c is the speed of light in air, we get n_e = 2.65, which is in good agreement with the value used in the design of microwave GaAs integrated circuits. From the measured standing wave pattern, we can evaluate the voltage standing wave ratio (VSWR) ρ and the reflection coefficient Γ of the GaAs CPW. The result is as follows: f_m =8.210 GHz, ρ = 5.97, and Γ = 0.71. The reason for ρ ≠ ∞ can be attributed to fringing field capacitance at the end of the transmission line and electrode losses.

Similar standing wave measurements were taken at different RF frequencies and with three different termination conditions (open, short, and 50Ω) (14). Figures 14a-c show the standing wave patterns in GaAs coplanar waveguide with open termination measured at 12.31, 16.41, and 20.10 GHz, respectively. The standing wave patterns of short, open, and 50Ω termination at 16.41 GHz are shown in Fig. 15a, b, and c, respectively. It should be noted that the position of termination is not accessible for the probing beam,

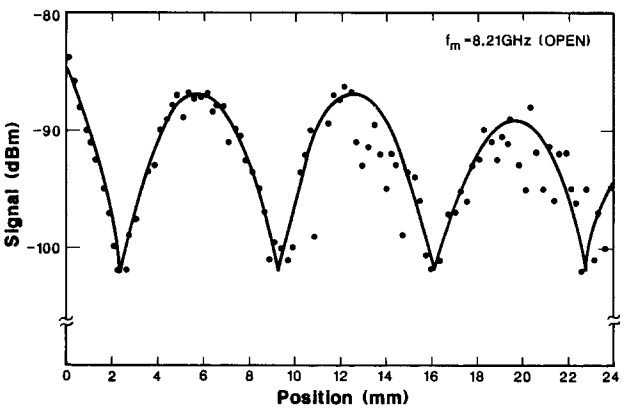

Fig. 13. Standing wave pattern in GaAs CPW with an open terminal (f_m = 8.21 GHz, f_o = 82 MHz, n = 100, and f_i = 10.7 MHz).

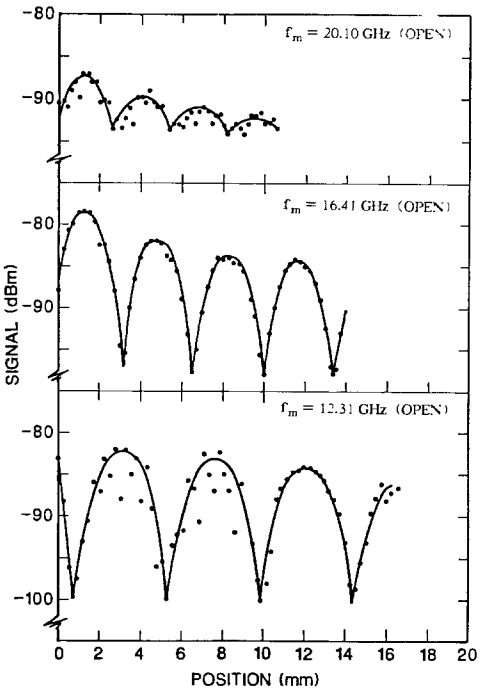

Fig. 14. Standing wave patterns in GaAs CPW with open terminals at frequencies of (a) 12.31, (b) 16.41, and (c) 20.10 GHz.

so the zero of abscissa in both figures is unknown. But we align three patterns by the positions of minima in Fig. 15 for purpose of comparison. The voltage standing wave ratios ρ's and the reflection coefficients Γ's calculated from these curves are listed in Table I.

From these data, first we can see that the values of the voltage standing wave ratios ρ's and the reflection coefficients Γ's decrease with increasing frequency due to the larger losses and stronger parasitic effects at higher frequencies. Second, the ρ and Γ with short termination are larger than those with open termination at 16.41 and 20.10 GHz, while they are not much different at 4.11 GHz. This indicates that the ideal open termination is more difficult to obtain than the ideal short termination at high fre-

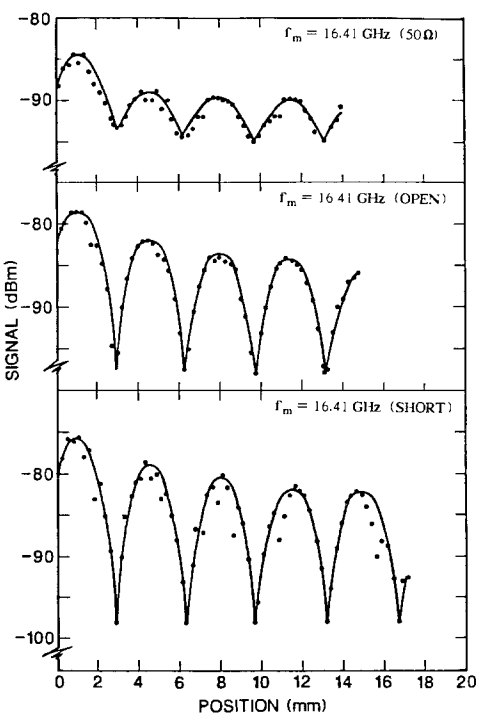

Fig. 15. Standing wave patterns in GaAs CPW with (a) short, (b) open, and (c) 50Ω terminations at 16.41 GHz.

Table I. Voltage standing wave ratio ρ and reflection coefficient Γ at frequencies up to 20.10 GHz

f_m (GHz)	ρ	Γ	Termination
4.11	12.4	0.85[1]	Open
	12.6	0.85[3]	Short
8.21[a]	5.97	0.71	Open
12.31	7.94	0.78	Open
16.41	5.95	0.71	Open
	9.41	0.81	Short
	1.90	0.31	50Ω
20.10	2.12	0.36	Open
	4.0	0.60	Short

[a] Data obtained from another sample with same geometry.

Table II. Standing wavelength λ_{sw}, effective dielectric constant ϵ_{eff}, and index of refraction n_{eff} at frequencies from 4.11 to 20.10 GHz

f_m (GHz)	4.11	8.21	12.31	16.41	20.10
λ_{sw} (mm)	13.60	6.90	4.60	3.45	2.80
ϵ_{eff}	7.20	7.01	7.02	7.02	7.10
n_{eff}	2.68	2.65	2.65	2.65	2.67
n'_{eff}	2.616	2.617	2.619	2.622	2.625

quency probably due to radiation loss. The ρ and Γ for 50Ω load are reasonably lower than those of open and short terminations.

From these experimental data, we also obtain the wavelength of standing wave λ_{sw} at frequencies from 4.11 to 20.10 GHz. Therefore, the effective dielectric constant ϵ_{eff} and refraction index n_{eff} can be calculated from λ_{sw}. They are summarized in Table II.

We see from Table II that the variation of n_{eff} is about 1% which is within the error of measurement. The experimentally deduced value can be checked against the value n'_{eff} calculated from the theoretical formula (27)

$$n'_{eff}(f) = \sqrt{\epsilon_{eff}(f)} = \sqrt{\epsilon_q} + \frac{(\sqrt{\epsilon_r} - \sqrt{\epsilon_q})}{(1 + aF^{-b})} \qquad [17]$$

where ϵ_q is the effective dielectric constant at the quasi-static limit, ϵ_r is the dielectric constant for GaAs, and $F = f/f_{TE}$, $f_{TE} = c/(4h\sqrt{\epsilon_r - 1})$. The values of the two constants a and b depend on the configuration and dimensions of the sample. In our case, the values of these parameters are as follow: $\epsilon_r = 13$, $\epsilon_q = 6.840$, $f_{TE} = 43.3$ GHz, $a = 24.81$, $b = 1.8$, $c = 3 \times 10^{10}$ cm/s, and $h = 500$ μm (substrate thickness). The calculated values of n'_{eff} for our sample in the frequency range from 4.11 to 20.10 GHz agree very well with the values of n'_{eff} deduced from our experimental results. From these data, we conclude that the dispersion of coplanar waveguide is negligible in this frequency range and $n_{eff} \approx 2.66$ for our sample dimension.

Discussion

The focusing lenses used in our experimental setup are specifically designed for laser focusing. Based on the data of the lens: the focal length = 14.5 mm, the aperture = 8.0 mm, the minimum spot size which we can get is about 1.4 μm. However, the actual diameter of the laser beam is about 6 mm, so that the actual minimum spot size ever obtained is about 1.9 μm. The laser beam spot with the radius of 2 μm is small enough for many applications of the electro-optic probing technique but is still too big for some special applications. For example, the field distribution of a FET with micrometer or submicrometer gate length is difficult to detect with the above spot size. We can choose a lens with a shorter focal length (larger numerical aperture) to reduce the spot size of laser beam to about 1 μm or less, but must be concerned with the problem of very short working distances for these lenses.

Because the laser beam is focused on the front side of the sample, the laser beam sweeps over a cone region in the sample. Besides, if the laser beam has a small incident angle with respect to the normal axis of sample surface, there is a transverse displacement between the incident beam and reflected beam (or transmitted beam). All of these factors degrade the spatial resolution. The former factor is hard to avoid but the latter one can be eliminated. As a whole, we can achieve spatial resolution up to 1 μm.

The lock-in detection is used in the CW electro-optic probing technique. The narrow bandwidth permits the measurement of weak signals in the presence of high noise, which could be many orders of magnitude larger than the signal. Therefore, very high measurement sensitivity can be achieved. The limit for us is for an integrating RC time constant of about 1s. In this case, the noise level caused by the laser diode and photodetector, etc., is about 1 μV, which gives the minimum detectable voltage. A detailed analysis of signal-to-noise ratio is given in Ref. (9).

Summary

The CW and pulsed electro-optic probing technique have been developed and their applications to investigation on the distribution of electric field, potential, and charge in GaAs semi-conductor material, device, and integrated circuit have been discussed. The experimental results on the field mapping, surface probing, and standing wave measurement demonstrate its capability and versatility. In addition to GaAs, electro-optic probing can be used to characterize InP, $LiNbO_3$, $LiTaO_3$, and other electro-optic materials, devices, and circuits. In particular, the pulse electro-optic probing with very broad bandwidth above 100 GHz will be an especially powerful method to characterize microwave and millimeter wave circuits.

Acknowledgments

This research is sponsored, in part, by the Joint Services Electronics Program contract F49620-87-C-0041 and the National Science Foundation grant ECE 8410838.

Manuscript submitted Oct. 29, 1987; revised manuscript received Oct. 20, 1988.

REFERENCES

1. J. A. Valdmanis, G. A. Mourou, and C. W. Gabel, *Appl. Phys. Lett.*, **41,** 211 (1982); *IEEE J. Quantum Electron.*, **QE-19,** 664 (1983).
2. B. H. Kolner, D. M. Bloom, and P. S. Cross, *Electron. Lett.*, **19,** 574 (1983).
3. K. E. Meyer, D. R. Dykaar, and G. A. Mourou, "Springer Series in Electrophysics," Vol. 21, p. 62, Springer-Verlag, New York (1985).
4. K. J. Weingarten, M. J. W. Rodwell, H. K. Heinrich, B. H. Kolner, and D. H. Bloom, *Electron. Lett.*, **21,** 765 (1985).
5. J. L. Freeman, S. K. Diamond, H. Fong, and D. H. Bloom, *Appl. Phys. Lett.*, **47,** 1083 (1985).
6. A. J. Taylor, R. S. Tucker, J. M. Wiesenfeld, C. A. Burrus, G. Eisenstein, J. R. Talman, and S. S. Pei, *Electron. Lett.*, **22,** 1068 (1986).
7. J. L. Freeman, S. R. Jefferies, and A. Auld, *Optics Lett.*, **12,** 795 (1987).
8. J. A. Valdmanis and G. A. Mourou, *IEEE J. Quantum Electron.*, **QE-22,** 69 (1986).
9. B. H. Kolner and D. M. Bloom, *ibid.*, **QE-22,** 79 (1986).
10. Z. H. Zhu, J-P. Weber, S. Y. Wang, and S. Wang, *Appl. Phys. Lett.*, **49,** 432 (1986).
11. Y. H. Lo, Z. H. Zhu, C. L. Pan, S. Y. Wang, and S. Wang, *ibid.*, **50,** 1125 (1987).
12. Z. H. Zhu, Y. H. Lo, S. Y. Wang, and S. Wang, Unpublished.
13. Z. H. Zhu, C. L. Pan, Y. H. Lo, M. C. Wu, and S. Wang, B. H. Kolner, and S. Y. Wang, *Appl. Phys. Lett.*, **50,** 1228 (1987).
14. Z. H. Zhu, M. C. Wu, Y. H. Lo, C. L. Pan, S. Y. Wang, and S. Wang, *J. Appl. Phys.*, (June 1988).
15. A. Yariv, "Quantum Electronics," John Wiley & Sons, Inc. New York (1975).
16. Y. H. Lo, M. C. Wu, Z. H. Zhu, S. Y. Wang, and S. Wang, *Appl. Phys. Lett.*, **50,** 1791 (1987).
17. S. Ramo, J. R. Whinnery, and T. Van Duzer, "Fields and Waves in Communication Electronics," John Wiley & Sons, Inc., New York (1976).
18. K. Horio, T. Ikoma, and H. Yanai, *IEEE Trans. Electron Devices*, **ED-33,** 1242 (1986).
19. S. Kakram-Ebeid and P. Minondo, *ibid.*, **ED-32,** 632 (1985).
20. M. F. Chang, C. P. Lee, D. L. Hou, R. P. Vahrenkamp, and C. J. Kirkpatrick, *Appl. Phys. Lett.*, **44,** 869 (1984).

21. M. S. Skolnick, M. R. Brozel, L. J. Reed, I. Grant, D. J. Stirland, and R. M. Ware, *J. Electron. Material*, **13,** 107 (1984).
22. F. Hasegawa, N. Yamamoto, and Y. Nannichi, *Appl. Phys. Lett.*, **45,** 461 (1984).
23. M. R. Brozel, I. Grant, R. M. Ware, and D. J. Stirland, *ibid.*, **42,** 610 (1983).
24. K. J. Weigarten, M. J. W. Rodwell, J. L. Freeman, S. K. Diamond, and D. M. Bloom, in "Ultrafast Phenomena V," G. R. Fleming and A. E. Siegman, Editors, pp. 98-102, Springer-Verlag, New York (1986).
25. M. J. W. Rodwell, M. Riaziat, K. J. Weingarten, B. A. Auld, and D. M. Bloom, *IEEE Trans. Microwave Theory Techniq.*, **MTT-34,** 1356 (1986).
26. B. H. Kolner, Ph.D. Thesis, Stanford University (1985).
27. G. Hasnain, A. Dienes, and J. R. Whinnery, *IEEE Trans. Microwave Theory Techniq.*, **MTT-34,** 738 (1986).

Rapid Thermal Alloyed Ohmic Contacts to p-Type GaAs

Yicheng Lu,[1] T. S. Kalkur, and C. A. Paz de Araujo*

Microelectronics Research Laboratories, Department of Electrical Engineering, University of Colorado, Colorado Springs, Colorado 80933-7150

ABSTRACT

A systematic study of Au/Zn/Au ohmic contacts to Be-implanted p-type GaAs by rapid thermal alloying is presented. The processing conditions, such as zinc composition and temperature-time cycle, are optimized. For the peak hole concentration, about $N_a = 3 \times 10^{17}$ cm^{-3}, contact resistivity as low as 3.3×10^{-6} Ω cm^2 is obtained. The microstructure of the contact is investigated using SEM, EDXA, AES, and XRD measurements in order to explore the correlation of the structural information with electrical characteristics represented by contact resistivity. It is found that during alloying, the GaAs layer near the interface is decomposed due to Ga and As outdiffusion, enhanced by Au interdiffusion. Ga diffuses to the contact surface in a much larger extent than As does. The interaction of Au and Ga, which produces α-AuGa phase, plays a key role in the formation of alloyed ohmic contacts to GaAs. The rapid thermal processing technique provides better control of Au-Ga reaction, as well as limited dissolution of the GaAs surface, which makes the optimum ohmic contact possible. The present work has demonstrated that rapid thermal alloying offers obvious advantages over the conventional furnace alloying process, including lower contact resistivity, better interface morphology by limiting interfacial liquid phase reaction, and controlled shallow penetration depth.

High quality ohmic contacts are necessary for the fabrication of GaAs devices, such as field effect transistors (FET), as well as a variety of optoelectronic devices. As GaAs devices are scaled down in dimensions and increased in complexity, the properties of ohmic contacts will greatly affect device performance and become one of the key factors in the evolution of GaAs processing technology. Ohmic contacts must have very low contact resistivity, smooth surface and interface morphology, sharp edge definition, and superior thermal stability. So far, most efforts have been concentrated on improving the ohmic contact quality of n-type GaAs (1, 2).

Recently, rapidly growing research has been focused on some GaAs devices which also require high quality p-type ohmic contacts. One such device is the heterojunction bipolar transistor (HBT), which has a structure that contains an n-type AlGaAs emitter, a p-type GaAs base, and an n-type GaAs collector (3, 4). High speed performance and reliability of these types of devices are directly related to the ohmic contact formed to the p-type base. Other new devices with p-type layers are p-channel heterostructure FETs, which can be combined with n-channel heterostructure FETs to form the complementary circuits (5, 6); and the complementary ion-implanted GaAs MESFETs (CMES), which are also attracting attention as components of ultra-high performance GaAs integrated circuits (7). For all of these p-channel FETs, high speed, low power dissipation and good noise immunity are greatly dependent on the quality of ohmic contact to p-type GaAs.

Unlike the commonly applied AuNiGe contacts to n-type GaAs, the ohmic contacts to p-type GaAs have not been systematically studied. The Au-Zn metallization system where zinc acts as acceptor is most commonly used for realization of alloyed ohmic contact to p-type GaAs. However, the Au-Zn alloy contacts are very hard to control and the contact resistivity is quite high, because Zn exhibits poor adhesion to GaAs, and the vapor pressure of Zn is much higher than that of Au. In order to overcome these problems, Au-Zn contacts can be prepared by electroplating (8) or sputtering (9). Sanada and Wade (10) report fairly reproducible furnace-alloyed Au/Zn/Au ohmic contacts to p-type GaAs. An empirical formula for the contact resistivity, using their technique, is expressed as $\rho_c = 1.8 \times 10^{18}\, p^{-1.3}$ Ω cm^2, where p(cm^{-3}) is the net hole concentration in the GaAs substrate. For $p = 3 \times 10^{17}$ cm^{-3}, which is equal to the doping level of the substrate used in the present investigation, ρ_c is about 3.4×10^{-5} Ω cm^2. Recently, Kaminska *et al.* (11) reported the interaction of Au/Zn/Zu contact layers with several III-V semiconductors, including GaAs, GaP, and InP. The effects of the alloying process on the composition and morphology of the contacts were studied with Rutherford backscattering (RBS), SIMS, and scanning electron microscopy (SEM). In their work, the substrate doping level is about 2×10^{17} cm^{-3}, and the reported ρ_c value is 6×10^{-4} Ω cm^2, which is fairly high. The optimization of the contact resistivity is necessary. The whole process of ohmic contact formulation is found to be very complex, and requires more investigation.

The conventional furnace alloying technique is not good enough to produce high quality ohmic contacts, which require low contact resistivity and good interface and surface morphology, as well as uniform and shallow penetration depth. In this paper, a systematic study of Au/Zn/Au ohmic contacts to Be-implanted p-type GaAs by rapid thermal alloying technique is presented. The alloying process is optimized to obtain the lowest contact resistivity. The microstructure of the contact is investigated by combining SEM, energy dispersive x-ray analysis (EDXA), Auger electron spectroscopy (AES), and x-ray diffraction (XRD) measurements to improve the understanding of the correlation between the structural and electrical characteristics. The advantages of the rapid thermal alloying process are discussed in comparison to the conventional furnace alloying technique.

Experimental

The wafers used in this study are semi-insulating (100) LEC GaAs substrates. The p-type conducting layers are formed by Be-implantation followed by rapid thermal annealing. The beryllium dose level is 8×10^{12} cm^{-2}, and the implantation energies are 50 and 100 keV, respectively. Nearly complete activation is achieved with the peak hole density of about 3×10^{17} cm^{-3}. For the isolation of the conducting channels used to measure the contact resistivities, a mesa etching was performed in a 1:10:10 H_2SO_4:H_2O_2:H_2O solution with an etching rate of 3 μm per min. The step depth was measured to be in the order of

*Electrochemical Society Active Member.
[1]Present address: Department of Electrical and Computer Engineering, Rutgers University, Piscataway, NJ 08855-0909